Research Article Vol. 5, No. 10 / October 2018 / Optica 1290

High-speed imaging of transient metabolic dynamics using two-photon fluorescence lifetime imaging microscopy

Andrew J. Bower,[1,2] Joanne Li,[1,3] Eric J. Chaney,[1] Marina Marjanovic,[1,3,4] Darold R. Spillman, Jr.,[1] and Stephen A. Boppart[1,2,3,4,*]

[1]Beckman Institute for Advanced Science and Technology, University of Illinois at Urbana-Champaign, 405 N. Mathews Ave, Urbana, Illinois 61801, USA
[2]Department of Electrical and Computer Engineering, University of Illinois at Urbana-Champaign, Urbana, Illinois 61801, USA
[3]Department of Bioengineering, University of Illinois at Urbana-Champaign, Urbana, Illinois 61801, USA
[4]Carle-Illinois College of Medicine, University of Illinois at Urbana-Champaign, Urbana, Illinois 61801, USA
*Corresponding author: boppart@illinois.edu

Received 10 July 2018; revised 31 August 2018; accepted 1 September 2018 (Doc. ID 338417); published 16 October 2018

Two-photon fluorescence lifetime imaging microscopy (2P-FLIM) of autofluorescent metabolic coenzymes has been widely used to investigate energetic perturbations in living cells and tissues in a label-free manner with subcellular resolution. While the currently used state-of-the-art instruments are highly sensitive to local molecular changes associated with these metabolic processes, they are inherently slow and limit the study of dynamic metabolic environments. Here, a sustained video-rate 2P-FLIM imaging system is demonstrated for time-lapse lifetime imaging of reduced nicotinamide adenine dinucleotide, an autofluorescent metabolic coenzyme involved in both aerobic and anaerobic processes. This system is sufficiently sensitive to differences in metabolic activity between aggressive and nonaggressive cancer cell lines and is demonstrated for both wide field-of-view autofluorescence imaging as well as sustained video-rate image acquisition of metabolic dynamics following induction of apoptosis. The unique capabilities of this imaging platform provide a powerful technological advance to further explore rapid metabolic dynamics in living cells.

https://doi.org/10.1364/OPTICA.5.001290

1. INTRODUCTION

Label-free optical metabolic imaging techniques capable of probing the energetic pathways within cells and tissues have had an important impact on understanding the role of metabolism in complex tissue microenvironments and in elucidating metabolic disorders associated with many diseases [1]. These techniques, based on the endogenous fluorescence of metabolic coenzymes, have shown great promise, for example, in investigating the tumor microenvironment [2] as well as in determining the efficacy of antitumor drugs at the cellular level [3]. In particular, two-photon fluorescence lifetime imaging microscopy (2P-FLIM), has been shown to be highly sensitive to the chemical and molecular environment of the fluorophore of interest [4]. When used to image nicotinamide adenine dinucleotide (NADH), an intrinsically fluorescent metabolic coenzyme, relative shifts in aerobic and anaerobic metabolism can be detected with high sensitivity based on the different fluorescence decay rates of unbound and mitochondrial-bound NADH [5]. This approach has been successfully used in several studies, such as identification of cell death processes both *in vivo* [6] and *in vitro* [7], and in a longitudinal investigation of the adverse effects following topical corticosteroid treatment in an *in vivo* mouse model [8].

Despite the wealth of information provided by 2P-FLIM for metabolic imaging, conventional methods for high-sensitivity imaging are burdened by slow acquisition rates. In modern 2P-FLIM, the most widely used detection method is known as time-correlated single-photon counting (TCSPC) [9]. With this method, the arrival times of single photons are individually recorded in reference to the excitation laser pulse to construct a histogram estimating the fluorescence decay profile. Due to the photon counting approach as well as the need for relatively low fluorescent photon count rates required for the detection electronics and a high number of collected photons for NADH imaging, TCSPC for NADH metabolic imaging has a speed restriction currently requiring pixel dwell times potentially on the order of 100 μs, limiting the study of dynamic metabolic microenvironments in point-scanning imaging approaches [1]. This approach has found broad adoption in two-photon fluorescence microscopy, where photon counting detection is commonly performed, and low count rates may be typical or acceptable due to the relatively weak two-photon absorption cross sections compared to single-photon fluorescence processes [10].

Recently, several strategies have been implemented to increase the throughput of 2P-FLIM systems by using analog measurements [11,12]. In particular, recent methods building upon direct

waveform recording techniques have been developed [12–14], which have previously seen use in single-photon fluorescence lifetime imaging [15]. These techniques have shown great promise in increasing the acquisition rate of 2P-FLIM at the cost of decreased lifetime sensitivity and signal-to-noise ratio (SNR) compared to TCSPC. However, this imaging approach has not been extended to NADH metabolic imaging of cells and tissues, which remains challenging compared to fluorescent tags or dyes due to the low fluorescence efficiency of NADH and the need for sensitive and accurate lifetime extraction to obtain metabolic contrast. In this study, a high acquisition-speed, label-free 2P-FLIM system is developed specifically to meet these challenges for NADH metabolic imaging and is used to investigate rapid changes in metabolic pathways in living cells and tissue, overcoming traditional speed limitations in high-resolution metabolic imaging and providing a unique tool to study transient metabolic dynamics with subcellular resolution.

2. MATERIALS AND METHODS

A. System Design

The system diagram of the developed high-speed 2P-FLIM system is shown in Fig. 1(a). The laser excitation is provided by a mode-locked Ti:Sapphire laser (Spectra-Physics Mai Tai HP) centered at 750 nm for NADH imaging. The beam is scanned across the sample by a galvo-scanning mirror (Cambridge Technology) for the slow axis and an 8 kHz resonant scanning mirror (EOPC SC-30) for the fast axis. For imaging, only data from the central portion of the resonant scanning mirror sweep were acquired to minimize distortions from the sinusoidal scan pattern. After the scanning mirrors, the beam is expanded through a 1:3 magnification telescope and focused by a high numerical aperture water-immersion objective (Olympus XLPLN-25X-WMP2—1.05 NA; 25× magnification) onto the sample. The emitted fluorescence light is collected by the same objective, reflected by a dichroic mirror, and passed through a bandpass fluorescence emission filter (450 ± 70 nm; Semrock Brightline FF01-450/70-25) onto an analog photomultiplier tube (PMT) (Hamamatsu H10721-20) operating at a gain level of approximately 10^6, ensuring that only fluorescence light from the sample is collected. The signal from the PMT is sent through a high bandwidth transimpedance amplifier (Hamamatsu C5594—1.5 GHz bandwidth) and directly digitized using a 12-bit, 1.8 gigasamples per second digitizer (AlazarTech ATS-9360).

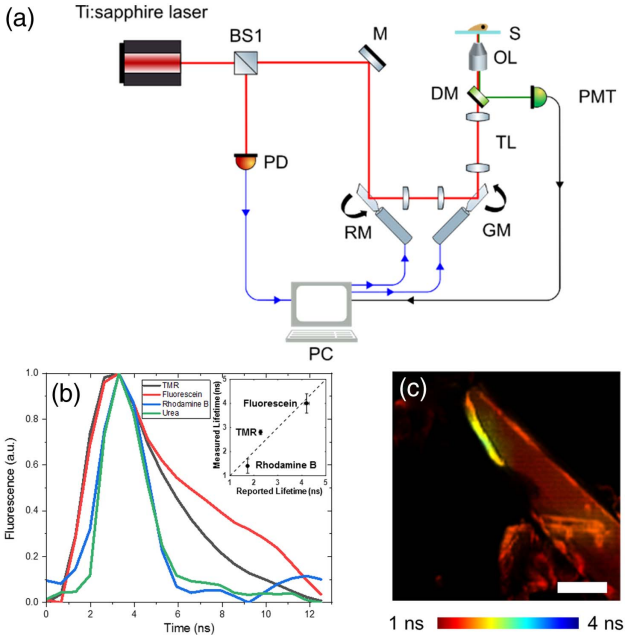

Fig. 1. High-speed 2P-FLIM system design and characterization. (a) System schematic of 2P-FLIM microscope; (b) representative fluorescence decay curves from standard fluorescent dyes. Inset plot shows comparison between extracted lifetime values compared to literature values for rhodamine B [16], 5' carboxytetramethyl rhodamine [17], and fluorescein [18]. (c) 2P-FLIM image of SHG signal from a urea crystal giving a measure of the response function of the system. Scale bar is approximately 10 μm. Abbreviations: BS, beam splitter; PD, photodiode; M, mirror; RM, resonant mirror; GM, galvo mirror; TL, tube lens; DM, dichroic mirror; OL, objective lens; S, sample; PMT, photomultiplier tube.

Direct synchronization of the digitizer sampling clock and scanning mirrors to the laser pulse repetition clock is necessary to ensure time-locked sampling of each image. The system clock is derived from the laser pulse train through direct measurement of the reflected beam by a 95/5 beam splitter using an amplified photodiode (ThorLabs PDB450A).

A 10 MHz reference clock obtained by downsampling the 80 MHz photodiode signal is provided to the digitizer, allowing synchronized control of the sampling rate that is phase-locked to the laser clock. An 8 kHz reference clock derived from the 10 MHz master clock is also provided to the resonant scanning mirror driver (EOPC PLD-1S) to ensure the synchronization between beam scanning and data acquisition. A high-speed fluorescence intensity imaging display is implemented in order to find important regions of interest and to preview the structural information of the acquired 2P-FLIM data sets. As data are acquired at GB/s rates, a high write-speed hard disk is needed for fast, sustained streaming of raw data to disk. This is accomplished using a peripheral component interconnect express (PCIE)-based solid-state hard drive (Samsung 960 Pro with sequential write speed up to 2.1 GB/s) taking the place of the traditional serial advanced technology attachment (SATA)-based hard disk. Utilizing the PCIE interface allows streaming of data from the digitizer to the solid-state drive without encountering a major RAM bottleneck, allowing video-rate recording of data over extended durations, limited only by the physical storage space of the solid-state drive capacity, allowing potentially hours of raw data streaming at video rate.

B. Data Analysis

For each pixel in an acquired image, a fluorescence lifetime decay curve is constructed by averaging the individual synchronized fluorescence decays over the pixel dwell time of the excitation pulses. Typically for NADH imaging, the fluorescence decay is modeled as a biexponential function and can be estimated from these measurements by performing nonlinear least squares curve fitting along with deconvolution of the instrument response function (IRF). However, this curve-fitting procedure can be challenging in the presence of large noise levels and for curves containing relatively few temporal data points.

When combined with the large total amount of data collected, fitting and deconvolution of these data with a biexponential model is somewhat impractical. In lieu of this, the data are directly fit from the peak response to a single exponential model, as has been performed in similar systems [12]. This is

subsequently cast as a linear least squares problem, taking the form of a large linear system of equations to solve for the fluorescence lifetime. When analyzed in this manner, a 2-min long acquisition at 20 fps (2400 data sets total) can be processed and analyzed in under 15 min using MATLAB, with much of this processing time spent on reading large data sets into memory. All data, excluding lifetime fitting from standard fluorescent dyes where deconvolution was performed, were processed in this manner. Finally, color-coding of the 2P-FLIM data was overlaid on the gray-scale fluorescence intensity images to coregister this structural and functional information.

C. Cell Culture

MCF-7 and MDA-MB-231 cells were plated in glass bottom imaging dishes (MatTek P35GC-0-14-C) in phenol red-free media (MEM alpha for MCF-7, Leibovitz's L-15 for MDA-MB-231) supplemented with 10% fetal bovine serum and antibiotics. Cells were imaged within 72 hours of plating based on confluency. All imaging was performed in ambient conditions at room temperature as all imaging in these studies was completed within 30 min.

To first assess the fluorescence lifetime contrast capabilities of the high-speed 2P-FLIM system, fluorescence decay curves were obtained from several standard fluorescent dyes including rhodamine B, 5' carboxytetramethyl rhodamine (TMR), and fluorescein [Fig. 1(b)]. Plots of these measured decays along with the IRF obtained through detecting second-harmonic generation (SHG) radiation from urea crystals show clear differences between the various fluorophores. To assess the accuracy of these measurements, the decays were deconvolved and fit to a single exponential model using the empirical IRF to obtain a lifetime measurement for each dye. The inset of Fig. 1(b) shows a direct comparison of the extracted lifetime values to previously reported values. The correlation between measured lifetime with this high-speed 2P-FLIM system and previously reported values indicates that the imaging system is capable of reliable lifetime contrast.

To demonstrate the imaging capabilities of this system, 256 pixel × 256 pixel 2P-FLIM images were acquired at 20 frames per second (fps) of urea crystals, which are known to produce SHG [Fig. 1(c)]. The crystal structure with short lifetime values corresponding to the near-instantaneous decay of the SHG process can be clearly visualized, confirming the high-resolution performance of this system.

3. RESULTS AND DISCUSSION

A. Large Field-of-View Imaging

To demonstrate the potential of this imaging platform for NADH metabolic imaging, Fig. 2 shows results of autofluorescence imaging of cells and tissue. A large field-of-view (FOV) 2P-FLIM mosaic was obtained from a 10 μm thick section of fixed rat testis tissue [Fig. 2(a)]. The acquisition was performed by acquiring a 10 × 10 mosaic of 250 μm × 250 μm FOV images, with approximately 30 averages per stage position recorded at 20 fps. These images were then merged together using MosaicJ, a stitching and blending plugin for ImageJ [19]. Previously in our lab, a similar mosaicking procedure was performed utilizing a TCSPC-based approach requiring approximately 3 h to acquire a 10 × 10 image mosaic [20]. Here, the full mosaic, spanning approximately 2 mm × 2 mm, was acquired in under 5 min, representing an approximately 36-fold increase in throughput for 2P-FLIM autofluorescence imaging.

It has been reported previously that the dominant autofluorescent components of this tissue are intracellular NADH and shorter lifetime elastin, present in the fibrous capsules surrounding the seminiferous tubules [21]. The shorter lifetime from elastin [Fig. 2(b), white arrows] can be clearly observed, compared to the longer lifetime of NADH. By constructing a histogram of lifetime values from the pixels in this mosaic, the presence of these two fluorophores can be clearly identified as a large, longer lifetime peak, belonging to NADH and a shorter lifetime shoulder due to elastin [Fig. 2(c), blue arrow]. The speed of this imaging procedure can be potentially increased even further, by extending the FOV of a single frame (using wider scan parameters) as well as averaging over a smaller number of images, trading off SNR for imaging speed.

B. *In Vitro* Metabolic Imaging

To determine the metabolic sensitivity of this system, *in vitro* cellular imaging was performed with two well-established breast cancer cell lines with distinct metabolic profiles, MDA-MB-231 [Fig. 2(d)] and MCF-7 [Fig. 2(e)]. Specifically, MCF-7 is a noninvasive, less aggressive cell line known to rely more on oxidative phosphorylation than the highly aggressive MDA-MB-231 cell line, which shows increased levels of aerobic glycolysis [22]. Imaging results using the high-speed 2P-FLIM microscope reveal a statistically significant increase in cytoplasmic NADH fluorescence lifetime in MCF-7 compared to MDA-MB-231 cells [Fig. 2(f)], showing clear sensitivity to the increased glycolytic activity in MDA-MB-231 cell line that has been reported previously [3]. Functional mapping of individual cells with this high-throughput imaging system can provide new insight into metabolic pathways in cells, and can be used to identify metabolic heterogeneity within complex cellular environments with the ability to sample a much larger number of cells than traditional TCSPC-based 2P-FLIM systems.

C. High-speed Metabolic Imaging of Cell Death Dynamics

To further demonstrate the capability of this system for tracking transient metabolic activity, the complex and dynamic process of apoptosis was investigated. Apoptosis, or programmed cell death, is an essential process in development and homeostasis in living organisms, and disruptions in metabolic pathways can lead to a variety of pathologies, including tumor development [23]. On the other hand, this form of cell death is often the desired outcome for a variety of commonly used anticancer therapeutic compounds, including doxorubicin and paclitaxel [24–26]. *In vitro* and *in vivo* studies of apoptosis suggest a strong early NADH lifetime response to apoptotic stimuli within minutes of treatment, but could not be further studied due to imaging speed limitations [6,7,27,28].

To further investigate this early response, the high-speed 2P-FLIM system was optimized for fast longitudinal imaging of living cells *in vitro*. Apoptosis was induced in MCF-7 cells with the addition of 5 μM staurosproine (STS) approximately 10 s following the start of 2P-FLIM imaging at 20 fps for a total duration of approximately 2 min (Fig. 3 and Visualization 1). Treatment with micromolar level doses of STS is well documented to efficiently

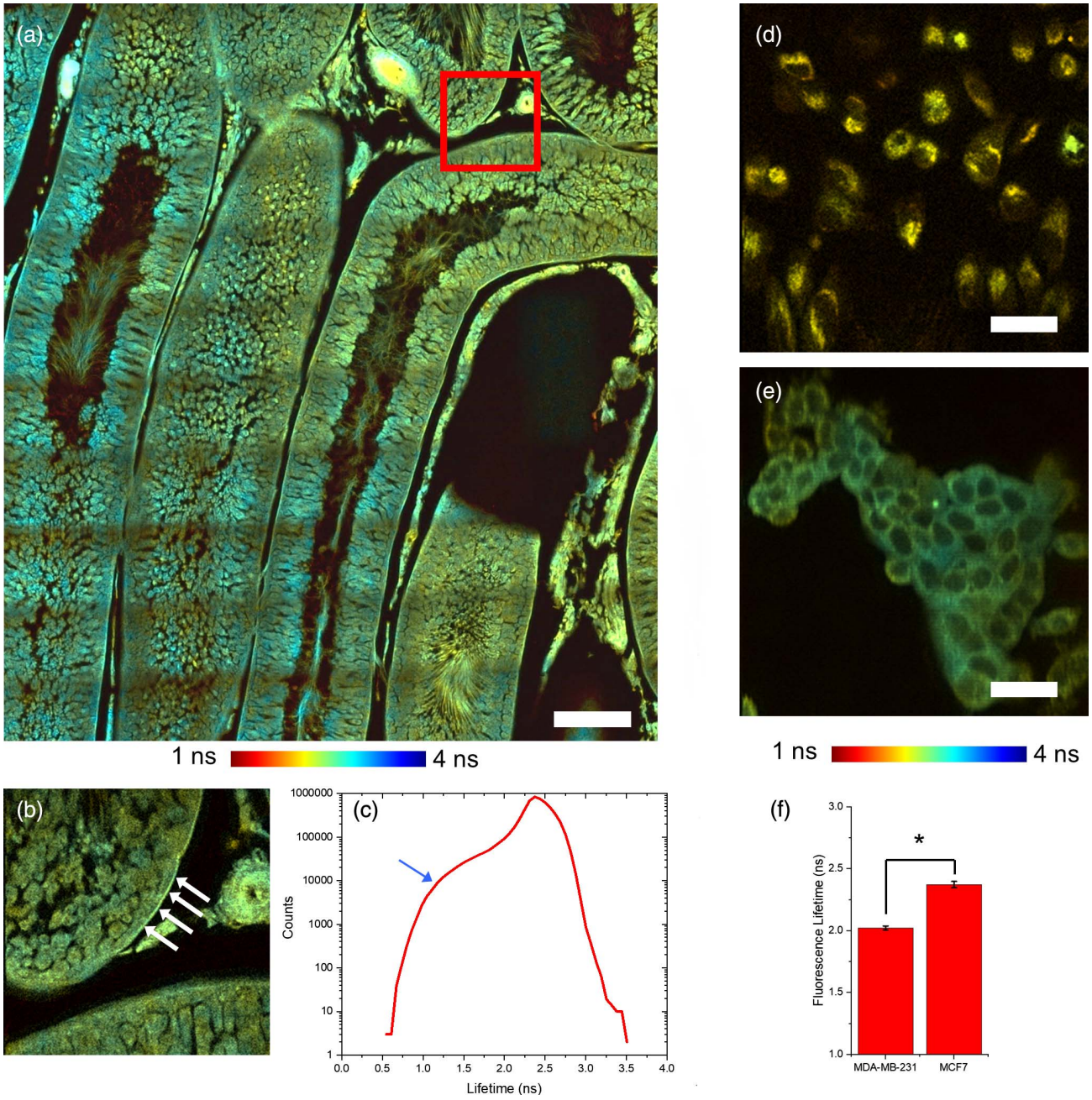

Fig. 2. High-throughput NADH 2P-FLIM imaging. (a) Wide FOV mosaic of a rat testis specimen acquired in under 5 min; (b) zoomed region from (a) corresponding to red box. White arrows correspond to elastin fluorescence from the fibrous cap of the seminiferous tubules. (c) Lifetime histogram of the acquired mosaic. The large peak corresponds to the NADH fluorescence, while the lower lifetime shoulder (blue arrow) corresponds to the elastin fluorescence. (d), (e) High-speed NADH 2P-FLIM images of (d) MDA-MB-231 and (e) MCF-7 cells; (f) statistical analysis comparing cytoplasmic lifetime from the two cell lines. Bar chart values represent mean ± s.e.m. ($N = 17$ for each group). Scale bar in (a) is 250 μm. Scale bar in (d), (e) is approximately 50 μm. $*p < 0.01$.

induce apoptosis in a large majority of the MCF-7 cell population [29,30]. Resulting images are displayed as averages over 20 frames.

Snapshots of both fluorescence intensity [Figs. 3(a)–3(c)] and lifetime [Figs. 3(d)–3(f)] at 0 s [Figs. 3(a) and 3(d)], 20 s [Figs. 3(b) and 3(e)], and 70 s [Figs. 3(c) and 3(f)] following the start of imaging show a statistically significant increase in both the fluorescence intensity [Fig. 3(i)] and lifetime [Fig. 3(j)] in analyzed single cells at 20 s that occurs on the order of seconds and persists for minutes following addition of STS. To reduce the effect of the background and nuclear regions during image analysis, the cell cytoplasm regions from each cell were extracted and used for quantification of fluorescence dynamics. Segmentation was performed using the software package CellProfiler [31] to isolate cell cytoplasm regions.

Immediately following the sharp increase after addition of STS, a decrease in NADH lifetime is observed, recovering to an elevated level compared to baseline [Fig. 3(h)]. Segmentation of NADH signals from the cell cytoplasm [segmentation map in Fig. 3(c)] shows statistically significant increases in both fluorescence intensity and lifetime comparing at 0 and 20 s using a

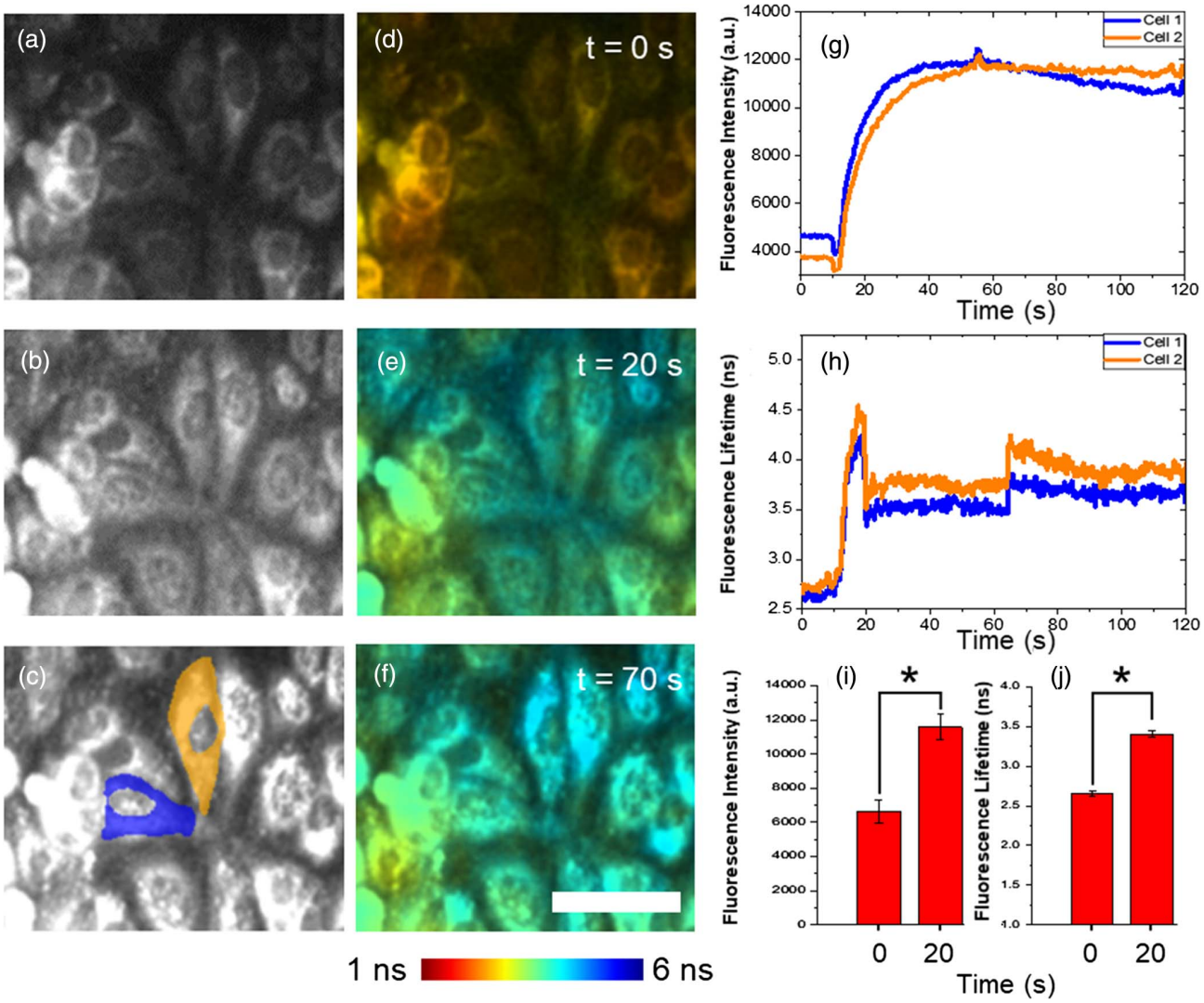

Fig. 3. High-speed 2P-FLIM of apoptosis induction in MCF-7 cells. (a)–(c) NADH intensity and (d)–(f) NADH lifetime images of apoptosis induction at time points of (a), (d) 0 s, (b), (e) 20 s, and (c), (f) 70 s. (g) NADH fluorescence intensity and (h) lifetime dynamics in cells 1 and 2 as labeled in (c). (i), (j) Comparison of NADH intensity (i) and lifetime (j) values at 0 and 20 s. Bar chart values represent mean ± s.e.m. ($N = 16$). Scale bar is approximately 50 μm. $*p < 0.01$.

two-sample t-test. These results suggest a dramatic increase in NADH production evidenced by the increase in NADH intensity [Fig. 3(g)] combined with dynamic changes in NADH binding provided by the high-speed time-resolved detection, indicating rapid shifts or disruptions to various steady-state metabolic pathways within seconds in response to the apoptotic-inducing stimuli. We hypothesize that the dramatic changes in the 2P-FLIM measurements seen at 20 and 70 s in this data set are related to the large dose of STS used to induce apoptosis, which may place a large energy burden on the cell, potentially leading to saturation of NADH binding to complex I in the mitochondria. Future study to further investigate the mechanism responsible for the observed dynamics is essential to understanding the relationship between apoptosis and dynamic changes in cell metabolism. It is important to note that this high-speed 2P-FLIM technique provides several benefits over high-speed two-photon fluorescence intensity microscopy approaches used previously for high-speed NADH imaging [32]. To begin, the fluorescence lifetime measurement is unaffected by fluorophore concentration providing highly specific metabolic information about the instantaneous binding status of NADH regardless of the absolute concentration. In addition, for deep-tissue imaging, this technique has the added benefit of being relatively insensitive to tissue absorption and scattering, which can have a noticeable effect on the collected fluorescence intensity signal. This high-speed metabolic imaging platform is thus capable of providing deeper insight into the strongly coupled interactions between metabolic pathways of the cell and the complex process of apoptosis at the earliest time points, currently impossible with commercially available metabolic microscopy platforms.

While this approach offers new capabilities for optical metabolic imaging, several challenges remain. Most importantly, measurement accuracy and temporal resolution are relatively low compared to TCSPC, which is much more sensitive to shorter fluorescence lifetime decays, and the effect of the IRF is diminished, leading to better fit results. In addition, biexponential decay fitting, which is crucial for extracting free- and protein-bound contributions of NADH fluorescence, currently remains a key

challenge with the high-speed 2P-FLIM system due to the low temporal resolution constrained by the speed of the digitizer. The fast imaging performed here, in addition with the weak fluorescence from NADH, increases the potential risk of photodamage. While no apparent photodamage was observed in the analyzed regions of the data sets shown here, laser parameters such as central wavelength, repetition rate, and pulse energy must be optimized and studied in the context of cell viability to know the effects of this imaging. Finally, while the acquisition speed of this system is increased compared to traditional TCSPC, the current processing techniques utilized prevent real-time display of 2P-FLIM images. This can be potentially overcome through the use of fast, parallel algorithms utilizing the graphics processing unit of the PC or the field-programmable gate array of a fast digitizer, potentially allowing high-speed biexponential fitting of fluorescence decay curves [11]. With increasing speeds of PC-based digitizers, as well as the incorporation of clever digitization schemes combined with utilization of fast, sensitive detectors such as multichannel plate PMTs, these issues can be resolved, increasing the sensitivity of the system while still permitting video-rate acquisition.

4. CONCLUSIONS

The high-speed 2P-FLIM system presented here has the potential to enable a variety of biological and clinical studies. This new approach provides an important tool for investigating a wide variety of highly dynamic metabolic processes and disorders in living cells. Further development of this technology could further enable important, but currently challenging tasks, such as high-throughput label-free metabolic cell screening, paving the way for a deeper understanding of the metabolic processes underlying complex cellular activity, which is important for both basic biological research and clinical translation of these discoveries.

Funding. National Institute of Biomedical Imaging and Bioengineering (NIBIB) (R01 EB023232); National Cancer Institute (NCI) (R01 CA213149); Air Force Office of Scientific Research (AFOSR) (FA9550-17-1-0387); National Science Foundation (NSF) (DGE-1144245); National Institutes of Health (NIH) (T32 EB019944).

Acknowledgment. A. J. B. was supported in part by a NSF Graduate Research Fellowship and by a Beckman Graduate Student Fellowship. J. L. was supported in part by an NIH T32 Tissue Microenvironment training grant. Schematic components in Fig. 1 were created using ComponentLibrary by Alexander Franzen (http://www.gwoptics.org/ComponentLibrary). Additional information can be found at http://biophotonics.illinois.edu. Ninety percent of the total project costs was financed with federal money and ten percent was financed by nongovernmental sources. The content is solely the responsibility of the authors and does not necessarily represent the official views of the National Institutes of Health.

REFERENCES

1. Z. Liu, D. Pouli, C. A. Alonzo, A. Varone, S. Karaliota, K. P. Quinn, K. Münger, K. P. Karalis, and I. Georgakoudi, "Mapping metabolic changes by noninvasive, multiparametric, high-resolution imaging using endogenous contrast," Sci. Adv. **4**, eaap9302 (2018).
2. M. C. Skala, K. M. Riching, A. Gendron-Fitzpatrick, J. Eickhoff, K. W. Eliceiri, J. G. White, and N. Ramanujam, "In vivo multiphoton microscopy of NADH and FAD redox states, fluorescence lifetimes, and cellular morphology in precancerous epithelia," Proc. Natl. Acad. Sci. USA **104**, 19494–19499 (2007).
3. A. J. Walsh, R. S. Cook, H. C. Manning, D. J. Hicks, A. Lafontant, C. L. Arteaga, and M. C. Skala, "Optical metabolic imaging identifies glycolytic levels, subtypes, and early-treatment response in breast cancer," Cancer Res. **73**, 6164–6174 (2013).
4. H. C. Gerritsen, M. A. H. Asselbergs, A. V. Agronskaia, and W. G. J. H. M. Van Sark, "Fluorescence lifetime imaging in scanning microscopes: acquisition speed, photon economy and lifetime resolution," J. Microsc. **206**, 218–224 (2002).
5. J. R. Lakowicz, H. Szmacinski, K. Nowaczyk, and M. L. Johnson, "Fluorescence lifetime imaging of free and protein-bound NADH," Proc. Natl. Acad. Sci. USA **89**, 1271–1275 (1992).
6. A. J. Bower, M. Marjanovic, Y. Zhao, J. Li, E. J. Chaney, and S. A. Boppart, "Label-free *in vivo* cellular-level detection and imaging of apoptosis," J. Biophoton. **10**, 143–150 (2017).
7. Y. Zhao, M. Marjanovic, E. J. Chaney, B. W. Graf, Z. Mahmassani, M. D. Boppart, and S. A. Boppart, "Longitudinal label-free tracking of cell death dynamics in living engineered human skin tissue with a multimodal microscope," Biomed. Opt. Express **5**, 3699–3716 (2014).
8. A. J. Bower, Z. Arp, Y. Zhao, J. Li, E. J. Chaney, M. Marjanovic, A. Hughes-Earle, and S. A. Boppart, "Longitudinal *in vivo* tracking of adverse effects following topical steroid treatment," Exp. Dermatol. **25**, 362–367 (2016).
9. W. Becker, A. Bergmann, M. A. Hink, K. König, K. Benndorf, and C. Biskup, "Fluorescence lifetime imaging by time-correlated single-photon counting," Microsc. Res. Tech. **63**, 58–66 (2004).
10. G. J. Brakenhoff, M. Müller, and R. I. Ghauharali, "Analysis of efficiency of two-photon versus single-photon absorption for fluorescence generation in biological objects," J. Microsc. **183**, 140–144 (1996).
11. J. Ryu, U. Kang, J. Kim, H. Kim, J. H. Kang, H. Kim, D. K. Sohn, J.-H. Jeong, H. Yoo, and B. Gweon, "Real-time visualization of two-photon fluorescence lifetime imaging microscopy using a wavelength-tunable femtosecond pulsed laser," Biomed. Opt. Express **9**, 3449–3663 (2018).
12. X. Y. Dow, S. Z. Sullivan, R. D. Muir, and G. J. Simpson, "Video-rate two-photon excited fluorescence lifetime imaging system with interleaved digitization," Opt. Lett. **40**, 3296–3299 (2015).
13. M. Eibl, S. Karpf, D. Weng, H. Hakert, T. Pfeiffer, J. P. Kolb, and R. Huber, "Single pulse two photon fluorescence lifetime imaging (SP-FLIM) with MHz pixel rate," Biomed. Opt. Express **8**, 3132–3142 (2017).
14. M. G. Giacomelli, Y. Sheikine, H. Vardeh, J. L. Connolly, and J. G. Fujimoto, "Rapid imaging of surgical breast excisions using direct temporal sampling two photon fluorescent lifetime imaging," Biomed. Opt. Express **6**, 4317–4325 (2015).
15. L. Marcu, "Fluorescence lifetime techniques in medical applications," Ann. Biomed. Eng. **40**, 304–331 (2012).
16. N. Boens, W. Qin, N. Basarić, J. Hofkens, M. Ameloot, J. Pouget, J.-P. Lefèvre, B. Valeur, E. Gratton, M. vandeVen, N. D. Silva, Y. Engelborghs, K. Willaert, A. Sillen, G. Rumbles, D. Phillips, A. J. W. G. Visser, A. van Hoek, J. R. Lakowicz, H. Malak, I. Gryczynski, A. G. Szabo, D. T. Krajcarski, N. Tamai, and A. Miura, "Fluorescence lifetime standards for time and frequency domain fluorescence spectroscopy," Anal. Chem. **79**, 2137–2149 (2007).
17. J. R. Unruh, G. Gokulrangan, G. S. Wilson, and C. K. Johnson, "Fluorescence properties of fluorescein, tetramethylrhodamine and Texas Red linked to a DNA aptamer," Photochem. Photobiol. **81**, 682–690 (2005).
18. D. Magde, G. E. Rojas, and P. G. Seybold, "Solvent dependence of the fluorescence lifetimes of xanthene dyes," Photochem. Photobiol. **70**, 737–744 (1999).
19. T. Philippe and U. Michael, "User-friendly semiautomated assembly of accurate image mosaics in microscopy," Microsc. Res. Tech. **70**, 135–146 (2007).
20. A. J. Bower, B. Chidester, J. Li, Y. Zhao, M. Marjanovic, E. J. Chaney, M. N. Do, and S. A. Boppart, "A quantitative framework for the analysis of multimodal optical microscopy images," Quant. Imaging Med. Surg. **7**, 24–37 (2017).
21. S. Vesuna, R. Torres, and M. J. Levene, "Multiphoton fluorescence, second harmonic generation, and fluorescence lifetime imaging of whole cleared mouse organs," J. Biomed. Opt. **16**, 106009 (2011).

22. R. A. Gatenby and R. J. Gillies, "Why do cancers have high aerobic glycolysis?" Nat. Rev. Cancer **4**, 891–899 (2004).
23. C. Thompson, "Apoptosis in the pathogenesis and treatment of disease," Science **267**, 1456–1462 (1995).
24. R. Gerl and D. L. Vaux, "Apoptosis in the development and treatment of cancer," Carcinogenesis **26**, 263–270 (2005).
25. A. V. Miller, M. A. Hicks, W. Nakajima, A. C. Richardson, J. J. Windle, and H. Harada, "Paclitaxel-induced apoptosis Is BAK-dependent, but BAX and BIM-independent in breast tumor," PLoS ONE **8**, e60685 (2013).
26. S. Wang, E. A. Konorev, S. Kotamraju, J. Joseph, S. Kalivendi, and B. Kalyanaraman, "Doxorubicin induces apoptosis in normal and tumor cells via distinctly different mechanisms," J. Biol. Chem. **279**, 25535–25543 (2004).
27. H.-W. Wang, V. Ghukasyan, C.-T. Chen, Y.-H. Wei, H.-W. Guo, J.-S. Yu, and F.-J. Kao, "Differentiation of apoptosis from necrosis by dynamic changes of reduced nicotinamide adenine dinucleotide fluorescence lifetime in live cells," J. Biomed. Opt. **13**, 054011 (2008).
28. J.-S. Yu, H.-W. Guo, H.-W. Wang, C.-H. Wang, and Y.-H. Wei, "Increase of reduced nicotinamide adenine dinucleotide fluorescence lifetime precedes mitochondrial dysfunction in staurosporine-induced apoptosis of HeLa cells," J. Biomed. Opt. **16**, 036008 (2011).
29. L. M. Mooney, K. A. Al-Sakkaf, B. L. Brown, and P. R. M. Dobson, "Apoptotic mechanisms in T47D and MCF-7 human breast cancer cells," Br. J. Cancer **87**, 909–917 (2002).
30. L.-Y. Xue, S.-M. Chiu, and N. L. Oleinick, "Staurosporine-induced death of MCF-7 human breast cancer cells: a distinction between caspase-3-dependent steps of apoptosis and the critical lethal lesions," Exp. Cell Res. **283**, 135–145 (2003).
31. A. E. Carpenter, T. R. Jones, M. R. Lamprecht, C. Clarke, I. H. Kang, O. Friman, D. A. Guertin, J. H. Chang, R. A. Lindquist, J. Moffat, P. Golland, and D. M. Sabatini, "CellProfiler: image analysis software for identifying and quantifying cell phenotypes," Genome Biol. **7**, R100 (2006).
32. A. M. D. Lee, H. Wang, Y. Yu, S. Tang, J. Zhao, H. Lui, D. McLean, and H. Zeng, "*In vivo* video rate multiphoton microscopy imaging of human skin," Opt. Lett. **36**, 2865–2867 (2011).